Pathway-specific deregulation of striatal excitatory synapses in LRRK2 mutations

Chuyu Chen[1], Giulia Soto[2], Nicholas Bannon[2], Shuo Kang[1], Yevgenia Kozorovitskiy[2#], Loukia Parisiadou[1#]

[1]Department of Pharmacology, Feinberg School of Medicine, Northwestern University, Chicago IL, USA; [2]Department of Neurobiology, Northwestern University, Chicago IL, USA

[#]Correspondence should be addressed to Yevgenia Kozorovitskiy and Loukia Parisiadou (yevgenia.kozorovitskiy@northwestern.edu, loukia.parisiadou@northwestern.edu)

ABSTRACT

LRRK2 is a kinase expressed in striatal spiny projection neurons (SPNs), cells which lose dopaminergic input in Parkinson's disease (PD). R1441C and G2019S are the most common pathogenic mutations of LRRK2. How these mutations alter the structure and function of individual synapses on direct and indirect pathway SPNs is unknown and may reveal pre-clinical changes in dopamine-recipient neurons that predispose towards disease. Here, R1441C and G2019S knock-in mice enabled thorough evaluation of dendritic spines and synapses on pathway-identified SPNs. Biochemical synaptic preparations and super-resolution imaging revealed increased levels and altered organization of glutamatergic AMPA receptors in LRRK2 mutants. Relatedly, decreased frequency of excitatory post-synaptic currents accompanied changes in dendritic spine nano-architecture, and single-synapse currents, evaluated using 2-photon glutamate uncaging. Overall, LRRK2 mutations reshaped synaptic structure and function, an effect exaggerated in R1441C dSPNs. These data open the possibility of new neuroprotective therapies aimed at SPN synapse function, prior to disease onset.

INTRODUCTION

Gain of function mutations in the leucine rich repeat kinase 2 (*LRRK2*) gene represent the most common cause of familial Parkinson's disease[1]. Carriers are at risk for late onset PD, which is clinically indistinguishable from sporadic PD, consistent with a possibility of common disease mechanisms[2,3,4,5]. *LRRK2* gene product is a large multi-domain protein with two catalytic domains: a GTPase (ROC-COR) domain and a serine/threonine-directed protein kinase domain. Pathogenic mutations are found predominantly in these two domains, suggesting that LRRK2 enzymatic activities are involved in PD pathogenesis[6,7]. Yet, how LRRK2 mutations in the two distinct functional domains contribute to PD pathogenesis and whether they act through a common mechanism is unknown. Enhanced LRRK2 kinase activity conferred by the G2019S (GS) mutation in the kinase domain is the most extensively studied property of mutant LRRK2[6,8]. Meanwhile, the R1441C (RC) substitution in the GTPase domain results in impaired GTP hydrolysis, which is thought to indirectly enhance kinase activity through mechanisms that remain to be determined[9,10].

Despite remaining questions, the last decade marks extensive progress in our understanding of LRRK2 function. This kinase is highly expressed in the spiny projection neurons (SPNs) of the striatum[9,11,12]. LRRK2 expression peaks in a developmental time window of extensive glutamatergic excitatory synapse formation, suggesting that LRRK2 may regulate the development or function of excitatory synaptic networks. Consistently, several lines of evidence suggest that loss of LRRK2 alters striatal circuits during postnatal development[12], and the GS pathogenic mutation increases glutamatergic activity in cultured cortical neurons[13] as well as in acute striatal slices[14,15]. Recent studies assign a critical role of LRRK2 in presynaptic terminal vesicle function[16]. Here, the GS mutation impairs presynaptic glutamatergic release, suggested to underlie changes in glutamatergic activity of striatal neurons[15]. The potential postsynaptic function of LRRK2 remains less well-characterized. We have previously shown that the RC mutation impedes normal striatal protein kinase A (PKA) signaling, which in turn results in increased GluA1 phosphorylation in developing SPNs, consistent with a postsynaptic mechanism of action[12]. Similarly, glutamate receptor trafficking perturbations were observed in *GS* knock-in (KI) mice in response to plasticity induction protocols[17]. Furthermore, although an increase in spontaneous excitatory postsynaptic currents has been reported for the dorsomedial striatum, a recent report failed to show this phenotype for the ventral striatum[18], despite LRRK2 expression in that region[19,20]. These observations suggest that LRRK2 mutations may shape the cortocostriatal synaptic function in a synapse-, cell- and area- specific manner. Overall, despite

the links between LRRK2 and glutamatergic synapse dysfunction, the field currently lacks a coherent framework for understanding how the two distinct LRRK2 mutations selectively alter synaptic function in specific cell types.

Given the complementary role of direct and indirect striatal pathways in behavior[21,22,23] the lack of pathway specificity in prior studies limits our understanding of disease related mechanisms associated with LRRK2 mutations. Previous studies did not compare the dysfunction of two LRRK2 mutations which are found in distinct LRRK2 domains and confer divergent biochemical properties to the kinase, choosing instead to focus on the one mutation or the other. Previous studies have mainly focused on the GS pathogenic mutation, and whether the molecular mechanisms underlying pathology across the two most common mutations remain unknown. In addition, the phenotype of LRRK2 mutant models is subtle and corresponds to a moderate susceptibility for PD. Therefore, refined tools are required to distinguish the early pre-pathology functional abnormalities. We have taken the approach of combining molecular, anatomical and electrophysiological approaches that capture global aspects of LRRK2 function in the striatum, but also single synapse specific effects, in case abnormalities are associated with specific synapse subtypes.

Here, we undertook a systematic synapse function and structure analysis in two different mutant LRRK2 mouse lines to evaluate the contribution of this kinase mutations to SPN synapses across direct and indirect pathways. Using a combination of subcellular fractionation biochemistry, super-resolution imaging, and 2-photon laser scanning microscopy with whole-cell physiology approaches, we found a critical role for LRRK2 RC, and to a lesser extent GS mutation, in organizing the structure and function of the SPN excitatory synapses, particularly for dSPNs.

RESULTS

LRRK2 +/*RC* mutation leads to increased synaptic incorporation of GluA1 in the striatum. In order to resolve LRRK2 mediated synaptic alterations in identified SPNs in a systematic way, we crossed the pathway-specific reporter BAC transgenic mice[24] with two mutant LRRK2 KI mouse lines. Specifically, *Drd1-Tomato* and *Drd2-eGFP* reporter mice were crossed with each of the two mutant LRRK2 lines (RC and GS) (**Figure 1A**). This platform enabled pathway specific interrogation of each LRRK2 mutation side by side, as well as initial experiments described below that were done on aggregated SPN populations. Our previous findings showed that *RC* KI neurons displayed altered PKARIIβ localization, as compared to wild-type (+/+) neurons, suggesting altered synaptic PKA activity in SPNs[12]. To further explore the synaptic PKA signaling

in both KI mouse lines, we employed differential centrifugation, discontinuous sucrose gradient, and detergent extractions to isolate synaptic subcellular fractions from striatal extracts as shown in **Figure 1B**[12,25,26]. Consistent with our previous data, PKA activity was found elevated in the P2 crude synaptosomal preparation of *+/RC* but not *+/GS* striatal extracts, when phospho-PKA substrate antibody was used to detect phosphorylation of downstream PKA targets. The increased PKA activity in *+/RC* was further confirmed by an increase in phosphorylation of GluA1, a key downstream target of PKA. It has been previously reported that Rab8A is a physiological target of LRRK2 kinase activity[8,27], but it is unknown whether this is the case in the striatum. We next investigated the contribution of each mutation to phosphorylation of Rab8A in the P2 striatal fractions. Notably, the RC, compared to the GS mutation, led to a stronger increase in Rab8A phosphorylation (**Figure 1D**). This finding stands in accordance with two recent studies in cell lines, showing that the RC and other mutations found in the GTPase domain of LRRK2 result in greater increase kinase activity, compared to the GS mutation[28,29]. We further isolated the post synaptic density (PSD) fraction from the P2 preparation by using a detergent extraction step. The PSD fraction showed enrichment of the postsynaptic marker PSD95, but not presynaptic protein synaptophysin (svp38) (**Figure 1C**). Given that PKA mediated phosphorylation of S845 in GluA1 has a significant impact on synaptic trafficking of GluA1[12,30], we examined the levels of GluA1 in the PSD fractions of KI mice. We observed a significant increase in the GluA1 levels in the PSD fraction from *+/RC,* but not *+/GS* mice, compared to wild type control (*+/RC:* 37.7% increase of control; *+/GS*: 2% increase relative to control, Kruskal-Wallis p=0.0092, post hoc tests as noted, n=4 per group) (**Figure 1E, F**), which was paralleled by elevated PKA activity specifically in the PSD fractions in *+/RC* (*+/RC*, 24.3 % of control, Kruskal-Wallis p=0.0194, post hoc tests as noted, n=4) but not *+/GS* mice (*+/GS*, 0.05% of control, n=4) (**Figure 1E, G**). Next, we determined the relative levels of PSD-95 protein in the PSD fraction across genotypes, which was used in the ratios in **Figure 1F, G**. We run subcellular fractions of all genotypes on the same blot (**Supplemental Figure 1A**), and normalized PSD95 to another synaptic protein, Homer1. PSD95 band intensities were expressed as fraction of the intensity of wild-type control S1 on the same blot (**Supplemental Figure 1B, C**). Furthermore, PSD95 band intensities in each of S1, P2, and PSD fractions were expressed as percentage of the PSD95 intensity of the wild type in each fraction. No differences in PSD95 levels in mutant LRRK2 fractions were observed after one way ANOVA. Overall, our data show increased GluA1 levels in the PSD fractions of *+/RC* striatal extracts, which parallels enhanced synaptic PKA signaling.

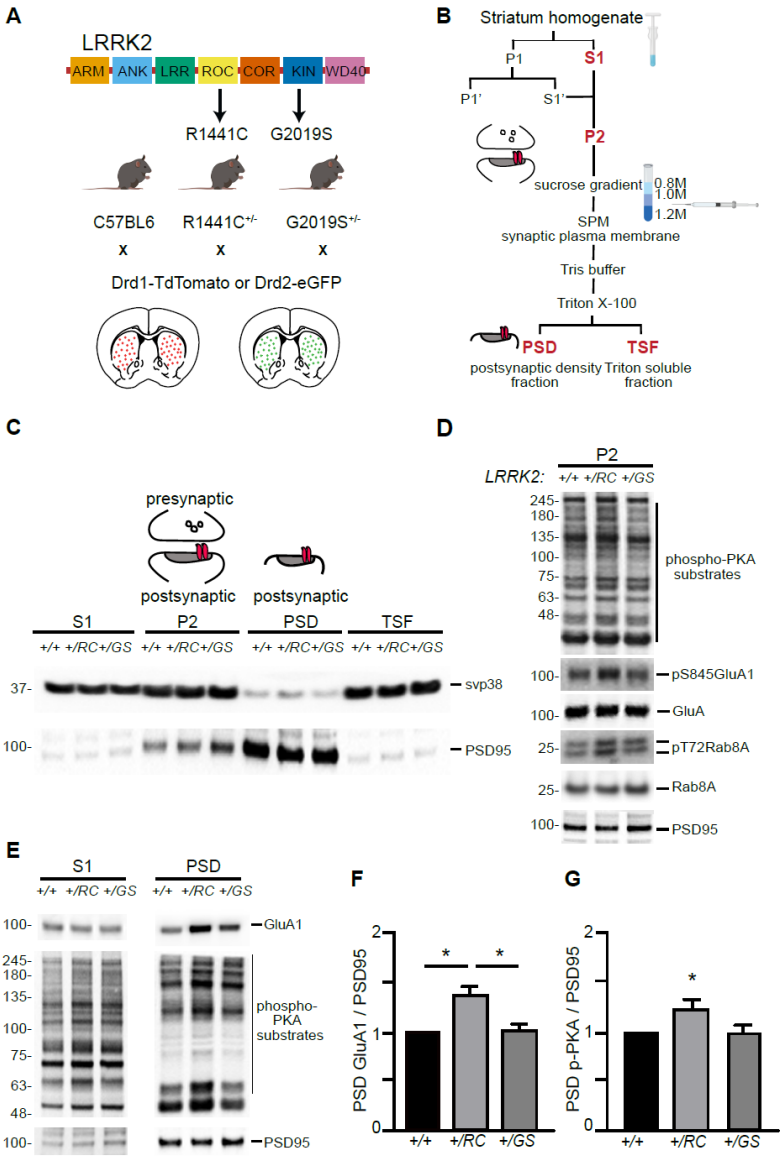

Figure 1. LRRK2 RC mutation increases synaptic glutamate receptor content in the striatum.

A. Schematic diagram of LRRK2 protein highlighting the armadillo repeats (ARM), ankyrin (ANK) repeats, Ras of complex (ROC), C-terminal of ROC (COR), kin (KIN), and WD40 domains. Knock- in mice expressing the R1441C and G2019S mutations found in the ROC and kinase domains respectively, crossed with either Drd1-Tomato or Drd2-eGFP mouse lines. **B**. Workflow schematic for subcellular fractionation of striatal homogenate for the enrichment of postsynaptic density fraction (PSD). **C**. Representative Western Blot analysis of the subcellular fractionation results, showing supernatant (S1), crude synaptosomal preparation (P2), PSD, and Triton soluble fractions (TSF). **D**. Western blot analysis of *+/+, +/RC*, and *+/GS* P2 striatal fractions probed for p-PKA substrates, pS845 GluA1, total GluA1, pT72Rab8, total Rab8, and PSD95. **E**. Western blot analysis of +/+, *+/RC*, and *+/GS* mice probed for GluA1, p-PKA, and PSD95. S1 and PSD fractions are shown. **F-G**. Quantification of GluA1 and p-PKA proteins in PSD fraction from **E** relative to control. Summary graphs reflect the mean, error bars reflect SEM. *p<0.05, Dunnet's post-hoc comparison following Kruskal-Wallis test.

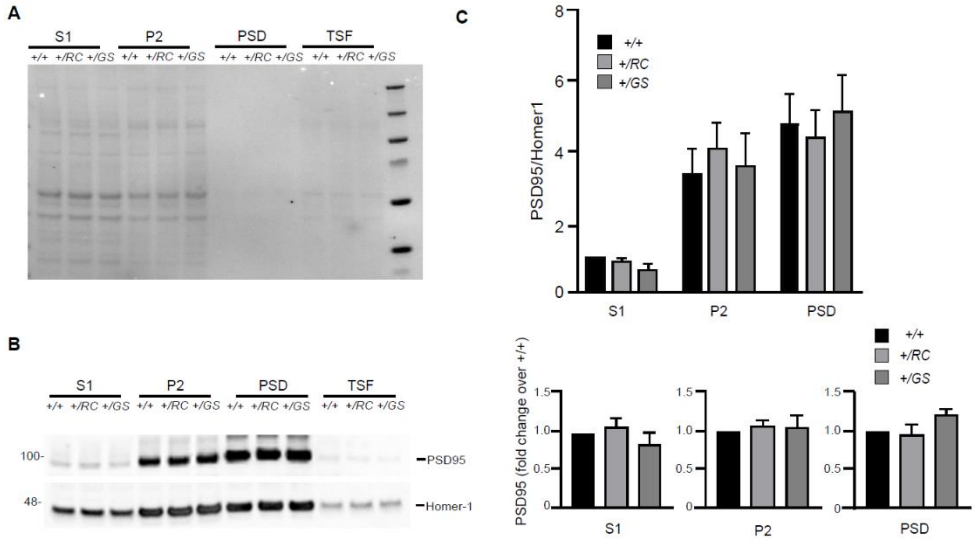

Supplemental Figure 1 related to Figure 1. A-B. Supernatant (S1), crude synaptosomal preparation (P2), PSD, and Triton soluble fractions (TSF) of wild type, +/RC and +/GS striata were run on the same blot. Ponceau staining shows similar loading across genotypes at a given fraction. Western blot analysis of the fractions described in **A**, probed for PSD95 and Homer-1. **C**. Quantification of PSD95 band intensities normalized to Homer-1. They are expressed as fraction of the intensity of the PSD95 intensity of S1 fraction of wild type controls. Summary graphs represent the mean, while error bars SEM. **D**. Quantification of PSD95 band intensities expressed as a fraction of the intensity of PSD95 wild type in each one of the S1, P2, and PSD95 fractions.

Altered nanoscale organization in the dendritic spines of direct and indirect pathway mutant LRRK2 SPNs

To precisely examine the nanoscale organization of GluA1 receptors in the dendritic spines of identified SPNs in mutant LRRK2 mice, we used structured illumination microscopy (SIM). SIM is able to overcome the resolution limits of conventional microscopy, and recently revealed a high degree of organization among scaffold proteins and AMPA receptors, forming nanoscale subsynaptic domains[31,32,33]. Primary cultured striatal neurons from *Drd1-dTomato* or *Drd2-eGFP* mice crossed with either +/*RC* or +/*GS* mouse lines (**Figure 2A**), were immunostained for GluA1 and PSD95 (**Figure 2B,** and **Figure 3A-B, Video S1**). We found several lines of evidence demonstrating increased synaptic incorporation of GluA1 in +/*RC* dSPNs, compared to +/+ ones. Specifically, the distance between GluA1 and PSD95 was smaller in +/*RC* dSPNs compared to control dSPNs, while no difference was observed between +/*GS* and +/+ neurons (+/RC, 63% of control, +/GS 85% of control one-way ANOVA, p=0.0208, post hoc tests as noted, n=75-93 dendritic spines/genotype) (**Figure 2C-D**). Similarly, the +/*RC* dendritic spines showed the greatest shift in cumulative distribution for minimum distance between GluA1 and PSD95

nanodomains (**Figure 2F**). While the overlap area of GluA1 and PSD95 nanodomains was found elevated in the dendritic spines of *+/RC* dSPNs, no differences were observed in *+/GS* neurons, compared to +/+ neurons (*+/RC*, 137% of control, +/GS, 102% of control one-way ANOVA p=0.0215, post hoc tests as noted, n=75-93 dendritic spines/genotype) (**Figure 2E)**. Similarly, the cumulative distribution analysis showed that GluA1-PSD95 distance was shifted towards higher values in the *+/RC* dSPNs (**Figure 2G**).

Given that the PSD95 area in *+/GS* dSPNs showed a trend towards decrease (+/RC, 94% of control, *+/GS*, 83% of control, one-way ANOVA p=0.0904, post-hoc +/+ vs +/GS p=0.075) (**Figure S2A, B**), we evaluated the percentage of the GluA1-PSD95 overlap relative to the total PSD95 area across genotypes. 32% of total PSD95 area contained GluA1 in *+/RC* dSPNs, compared to 23% in +/+ neurons, and 26% in *+/GS* neurons (one way ANOVA p=0.0015, post hoc tests as noted) (**Figure 2H**). These data strongly suggest increased levels of GluA1 at the synapses of +/RC dSPNs. Correlation analysis was performed to investigate the association between GluA1-PSD95 overlap nanodomain area and PSD95 area. A positive correlation was observed in all three genotypes (control, Spearman r=0.5822, p-value<0.0001, +/RC, r=0.6522, p<0.0001 and +/GS r=0.6569, p-value<0.0001). The correlation was stronger in LRRK2 mutant SPNs (**Figure 2I-K**).

A similar synaptic nanoscale organization analysis was performed for *Drd2-eGFP* control and mutant LRRK2 SPNs. The neurons were immunostained with GluA1 (purple), and PSD95 (orange) (**Figure 3A-B**) and minimum distance summary data (*+/RC*, 87% of control, *+/GS*, 89% of control, one-way ANOVA, p=0.6435 n=72-88 dendritic spines/genotype), as well as cumulative distribution of the distance between the GluA1 and PSD95 nanodomains, showed no difference across genotypes (**Figure 3C-D, F**). We observed that the overlap GluA1 and PSD95 area was increased in *+/GS* SPNs (*+/RC*, 105% of control, *+/GS*, 155% of control, one-way ANOVA, p<0.0001; post hoc tests as noted, p=72-88 dendritic spines/genotype) (**Figure 3E**). Further analysis showed an increase in the mean PSD95 area in the *+/GS* neurons (*+/RC*, 123% of control, *+/GS*, 137% of control, one-way ANOVA, p=0.0008, post hoc tests as noted) (**Supplemental Figure 2C**), as well as in cumulative frequency (**Supplemental Figure 2D**). However, the percentage of the total PSD95 area containing GluA1 nanodomains *+/GS* iSPNs compared to controls was similar (one-way ANOVA, p=0.469) (**Figure 3H**). Thus, the increased size of GluA1-PSD95 overlapping domains in the *+/GS* iSPNs reflects the elevated PSD95 area of these neurons (**Supplemental Figure 2C-D**), and not synaptic GluA1 incorporation, as found in *+/RC*.

We aimed to further investigate the relationship between overlapping nanodomains size and PSD95 area in the iSPNs dendritic spines. In general, PSD95 area correlated with the overlap GluA1-PSD95 domain size in all genotypes (control, Spearman r=0.7817, p<0.0001, +/RC, r=0.3996, p=0.0003 and +/GS, r=0.6938, p<0.0001) (**Figure 3I-K**). Based on **Figure 2I,** we found that for larger PSD95 domains, mutant LRRK2 dSPNs show a tendency towards larger overlap between GluA1 and PSD95. However, this was not the case for iSPNs of *+/RC* genotype. In fact, in *+/RC* iSPNs, some high overlap GluA1-PSD95 domains were characterized by smaller PSD95 areas. This detailed high resolution imaging analysis points to different GluA1 subsynaptic distribution in the iSPNs of *+/RC* SPNs, compared to +/+ and *+/GS*. Taken together, these single synapse imaging findings in pathway identified SPNs demonstrate an increased number of GluA1 receptors in the synapses of *+/RC* dSPNs, pointing towards cell type and mutant specific LRRK2 functions. These observations suggest highly specific and likely regulated nanoscale organization of GluA1 receptors in SPN dendritic spines.

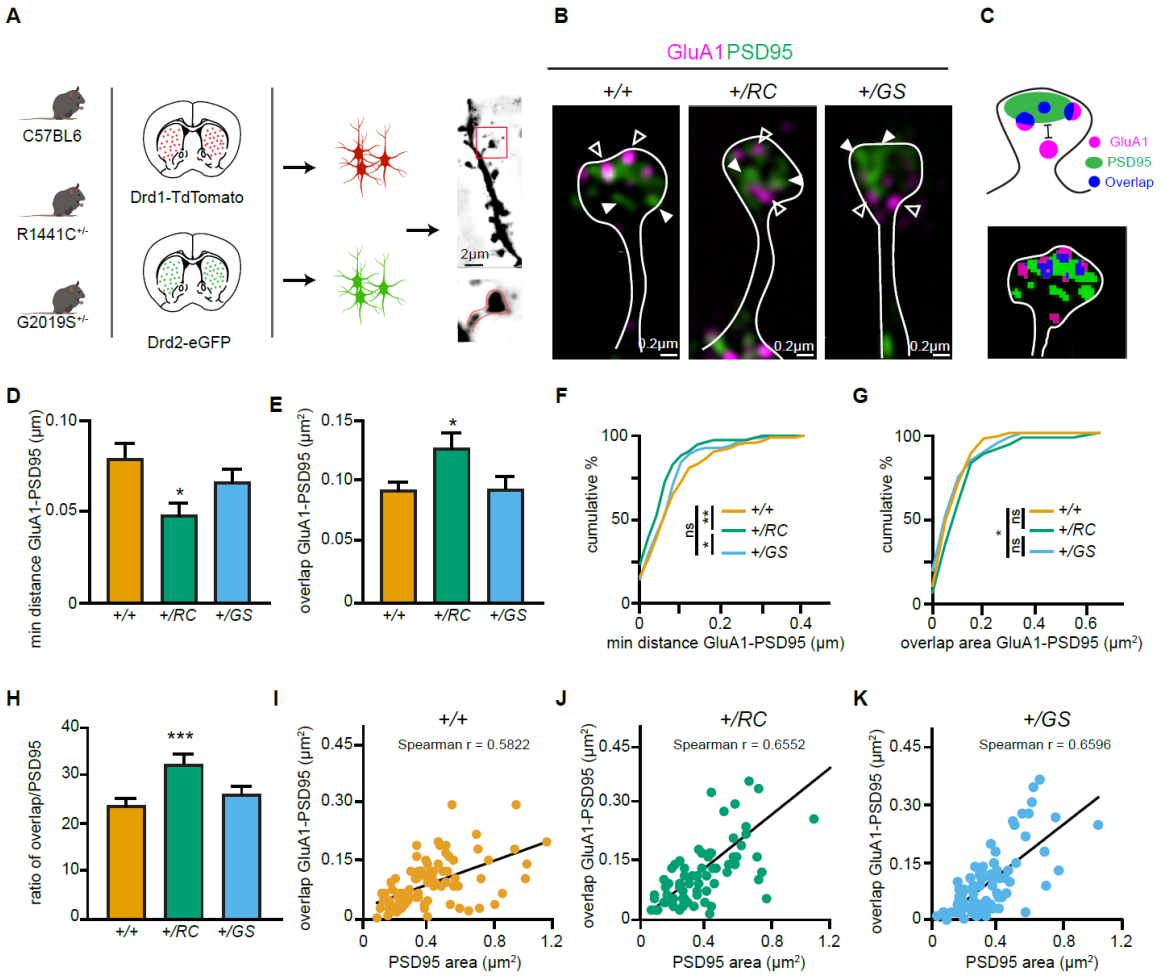

Figure 2. LRRK2 RC mutation restructures the nanoscale synaptic organization of dSPNs.

A. Schematic depicting experimental design. **B.** Structured Illumination super-resolution microscopy (SIM) image of dendritic spines on *+/+, +/RC*, and *+/GS Drd1-Tomato* expressing SPNs, labeled with antibodies to GluA1 (purple), and PSD95 (green). Open arrowheads, GluA1 nanodomains; arrowheads, PSD95 nanodomains. **C**. Schematic diagram and object masks depicting GluA1, PSD95, and overlap nanodomains within a dendritic spine. Minimum distance between GluA1-PSD95 is measured from the closest edge of the two nanodomains, as shown. **D**. Summary graphs showing the minimum distance between GluA1 and PSD95 nanodomains. Asterisks reflect statistical significance for Tukey'smultiple comparison tests after one way ANOVA. **E**. Same as **D,** but for the overlap area of GluA1 and PSD95 nanodomains within dendritic spines. **F-G**. Cumulative distribution of the data shown in **D** and **F**. Asterisks show statistical significance for Bonferroni post hoc comparisons after Kolmogorov-Smirnov tests. **H**. Bar graphs showing the ratio of GluA1-PSD95 overlap area in **E** relative to PSD95 area, across genotypes. Data are represented as mean±SEM. **I-K**. Correlation plots of overlap in GluA1-PSD95 area versus PSD95 area for *+/+, +/RC*, and *+/GS* Drd1-Tomato expressing SPNs. *p<0.05, **p<0.01, ***p<0.001.

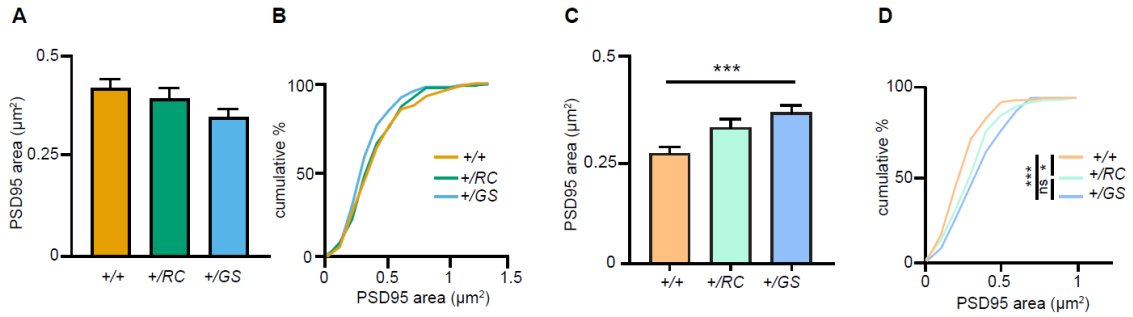

Supplemental Figure 2 related to Figures 2 and 3. A. Summary graph, PSD95 area across genotypes of dSPNs. Error bars reflect SEM. **B**. Cumulative percentage of PSD95 area per dendritic spine across dSPN genotypes. **C**. Summary graph, PSD95 area across genotypes of iSPNs. Error bars reflect SEM; asterisks, Tukey post hoc comparisons after one-way ANOVA, +/+ vs. *+/GS p<0.001* **D.** Cumulative percentage of PSD95 areas per dendritic spine across iSPN genotypes**.**

Video S1, related to **Figure 2**. 3D Reconstruction of dendritic spine of an RC dSPN. GluA1 (purple), and PSD95 (green), overlap area (white), as in **Figure 2B**. A surface mask is added for a fraction of the video, enabling the visualization of GluA1 and PSD95 in spine head.

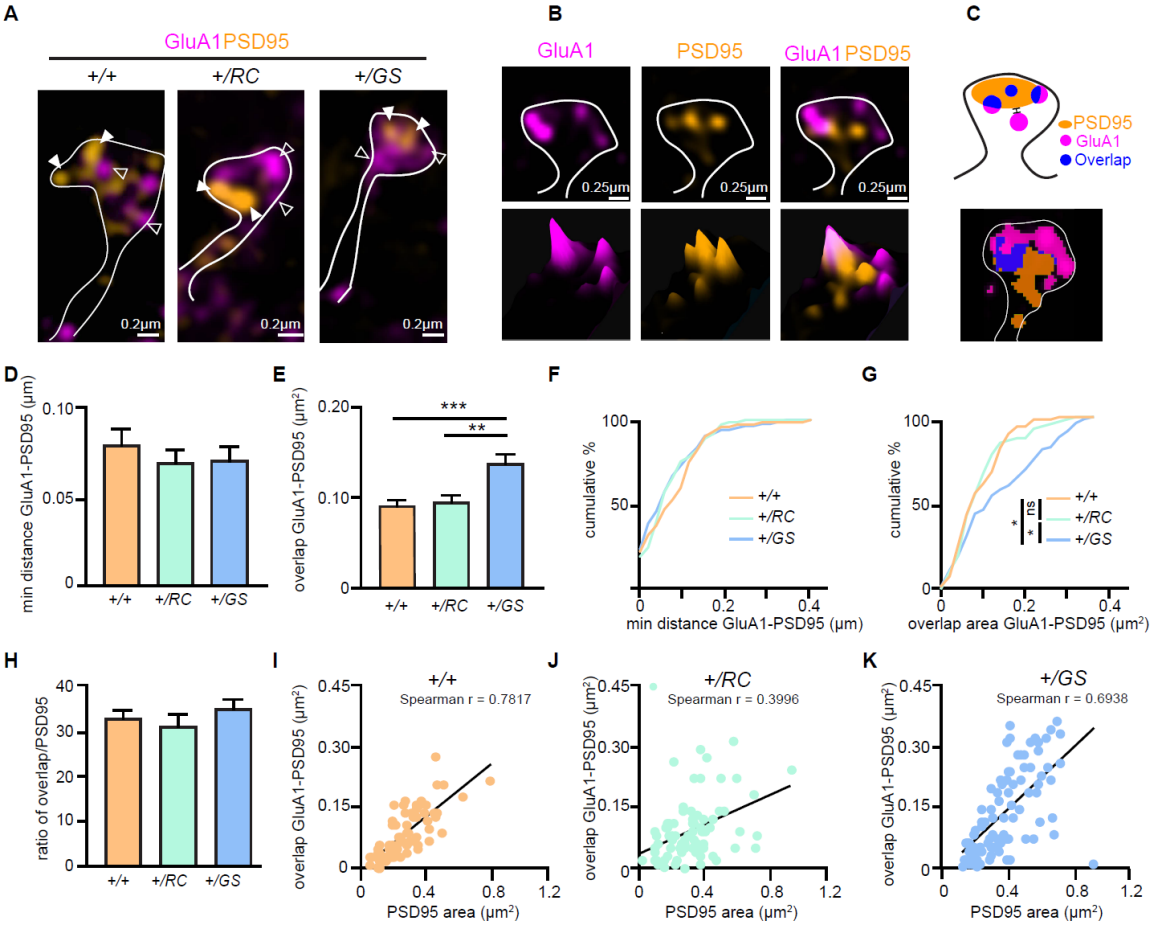

Figure 3. LRRK2 mutations alter the nanoscale synaptic organization of iSPNs.

A. SIM image of *+/+, +/RC*, and *+/GS* Drd2-eGFP expressing SPNs immunostained with GluA1 (purple), and PSD95 (orange). Open arrowheads, GluA1 nanodomains; arrowheads, PSD95 nanodomains. GFP antibody was used to amplify the Drd2-eGFP signal. **B**. Surface intensity through a dendritic spine head in an RC iSPN. **C**. Schematic diagram and object masks depicting GluA1, PSD95, overlap nanodomains, and minimum distance between nanodomains within a dendritic spine head. **D.** Bar graphs showing the minimum distance between GluA1 and PSD95 nanodomains. **E.** Summary data showing the overlap area between GluA1 and PSD95 nanodomains in dendritic spine heads across genotypes. Asterisks show statistical significance for Tukey's multiple comparison tests after one way ANOVA. **F-G**. Cumulative distribution of data shown in **D** and **E**. Asterisks reflect statistical significance for Bonferroni post hoc comparisons after Kolmogorov-Smirnov tests. **H**. The ratio of overlap area between GluA1 and PSD95 to the PSD95 area for *+/+, +/RC*, and *+/GS* iSPNs **I-K**. Correlation plots of overlap areas versus PSD95 area for iSPNs across genotypes. *p<0.05, **p<0.01, ***p<0.001.

Pathway specific functional alterations in the synapses of R1441C and G2019S SPNs

Since the effects of LRRK2 mutations appear to alter excitatory synapse subunits, next we carried out recordings of pharmacologically isolated miniature excitatory post-synaptic currents (mEPSCs) in acute brain slices from mice of the three genotypes. SPN pathway identity was determined based on the presence or absence of Drd2-eGFP[34]. Neurons were held at -70 mV in voltage clamp, and mEPSCs were recorded in the presence of tetrodotoxin (TTX). For dSPNs, frequency of mEPSCs decreased relative to controls for both LRRK2 mutations (GFP-, RC 60% of control, GS, 47% of control; two-way ANOVA, genotype main effect, $p<0.001$, post hoc tests as noted) (**Figure 4A-B**). For iSPNs, an analogous decrease in the frequency of mEPSCs was observed in both RC and GS neurons (GFP-, RC 60% of control, GS, 52% of control; two-way ANOVA, genotype main effect, $p<0.001$, post hoc tests as noted). In contrast to frequency of mEPSCs, no changes in amplitude were observed across all six genotype/cell type combinations on post hoc comparisons, despite a modest main effect of genotype (GFP-, RC 107% of control, GS, 92% of control; GFP+, RC 108% of control, GS 94% of control; two-way ANOVA, genotype main effect, $p=0.041$, N=13-14 neurons/group) (**Figure 4C**). To evaluate the distribution of individual mEPSC features across genotypes, we computed cumulative distributions of inter-event intervals (IEIs) and amplitudes (**Figure 4D-E**). The distribution of mEPSC IEIs in LRRK2 mutants differed from controls for both pathways, with a greater proportion of larger IEIs, consistent with differences in mEPSC frequency. In addition, the distribution of mEPSC amplitudes in RC dSPNs was shifted towards larger events.

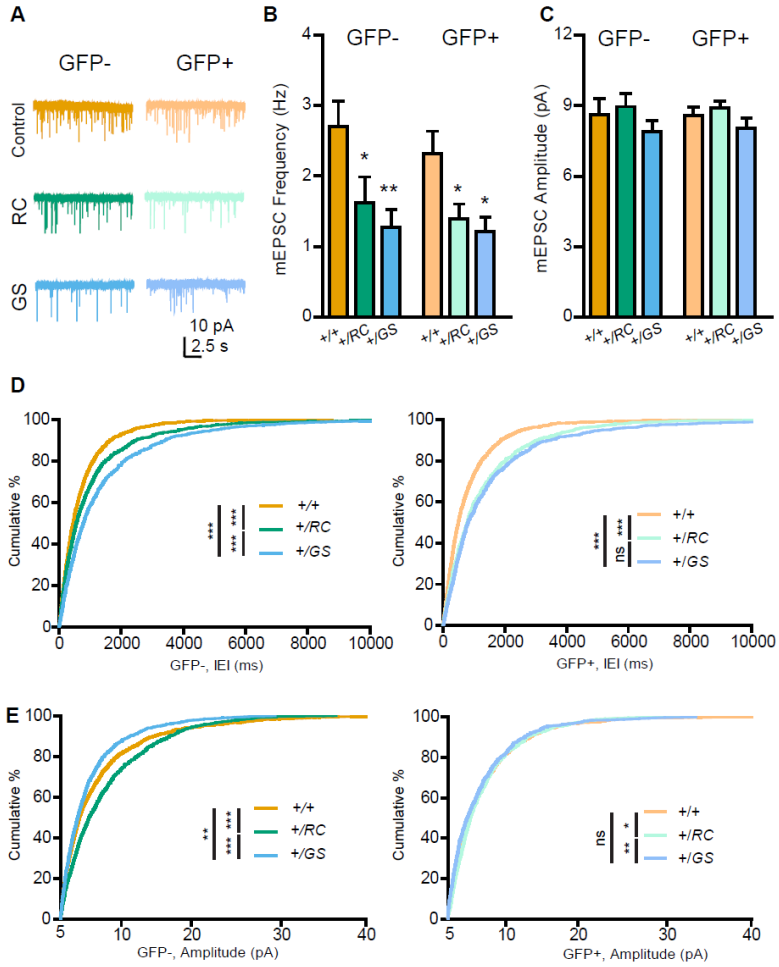

Figure 4. Pathway-specific functional alterations of SPN synapses in LRRK2 mutants.

A. Example miniature excitatory postsynaptic current (mEPSC) traces from individual neurons of 6 genotype-pathway combinations. GFP-, dSPNs; GFP+, iSPNs; color, as defined in the figure. Scale bars, 10 pA and 2.5 seconds. **B**. Summary graph showing the frequency of pharmacologically isolated mEPSCs, in GFP- and GFP+ SPNs in controls, compared to both RC and GS mutations. Asterisks reflect statistical significance for Bonferroni post hoc comparisons after two way ANOVA. **C**. Same as **B**, but for mEPSC amplitude. **D**. *Left*, cumulative distribution of inter-event intervals (IEI) for mEPSCs across genotypes for GFP- SPNs. *Right*, same as *left*, but for GFP+ SPNs. X axis starts at 5 pA, reflecting the amplitude threshold for mEPSC identification. Asterisks reflect statistical significance for Bonferroni post hoc comparisons after Kolmogorov-Smirnov tests. **E**. Same as **D**, but for cumulative distributions of individual event amplitudes. *p<0.05, **p<0.01, ***p<0.001.

Overall dendritic spine density and morphology is conserved in mutant LRRK2 SPNs

To investigate whether the observed decrease in the mEPSC frequency was associated with global changes in dendritic spine number and morphology, we relied on identifying pathway specific SPNs by injecting a Cre dependent adeno-associated virus (AAV) expressing eGFP virus (AAV8/Flex-GFP) in the striatum of neonatal pups. *Drd1-Cre* and *Adora2a-Cre* mice were crossed with *+/RC* and *+/GS* mice, as well as controls (**Figure 5A**, **Video S2**). We then analyzed dendritic fragments of d- and iSPNs to determine dendritic spine density, spine head width, and spine length. No differences in any of these parameters were observed for all six genotype/cell type combinations (two-way ANOVA, n=9-12 SPNs from 3-4 mice/genotype) (**Figure 5B-E)**. Further dendritic spine classification showed no difference in dendritic spine type in SPNs of either pathway (two way ANOVA, n=9-14 SPNs for 3-4 mice/genotype) (**Figure 5F**). Overall, these data suggest that the functional synaptic alterations (**Figure 4**) observed in *+/RC* and *+/GS* mutant SPNs are not reflected in uniform changes in dendritic spine number or morphology.

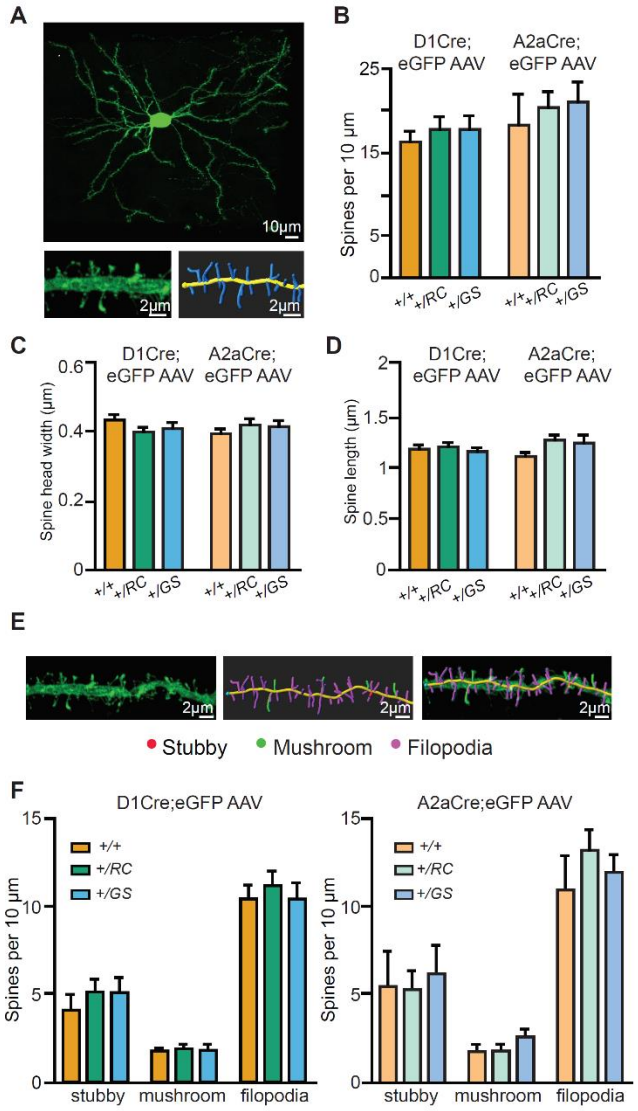

Figure 5. Pathway-specific analysis of dendritic spine morphology in LRRK2 mutants.

A. Example confocal maximum projection image of a *+/RC;Adora2a-Cre* iSPN expressing AAV8/Flex-GFP. Representative dendritic fragment with dendritic spines and the corresponding 3D Imaris generated filament. **B**. Summary graph showing the dendritic spine density in pathway-identified SPNs across genotypes. Quantification of dendritic spine head width (**C**), and dendritic spine length (**D**) in d- and iSPNs. **E**. Confocal maximum projection image and the corresponding 3D Imaris generated filament with classified dendritic spines. Red, stubby; green, mushroom; purple, filopodia. **F**. *Left*, summary data showing the density of each dendritic spine category in dSPNs. *Right*, same as left, but for iSPNs.

Video S2, related to **Figure 5**. 3D Reconstruction of an identified *+/RC;Adora2a-Cre* (Drdr1-, iSPN) neuron transduced with a Cre dependent AAV eGFP virus (AAV8/Flex-GFP) in neonatal pups.

Enhanced single synapse glutamate uncaging-evoked currents in dSPNs of LRRK2 R1441C mutant SPNs

Our results indicate that the abundance of GluA1 subunits is selectively increased in dendritic spines of *+/RC* dSPNs, along with synaptic AMPAR presence and the prevalence of larger amplitude mEPSCs. This is consistent with a possibility that a specific fraction of *+/RC* excitatory synapses are functionally stronger. In order to evaluate the physiology of single dendritic spines in pathway-identified SPNs across three genotypes, we used 2-photon dual laser glutamate uncaging and imaging, combined with whole-cell electrophysiology in voltage clamp mode (**Figure 6A**). *Drd2-eGFP* mice were crossed into G2019S and R1441C KI lines, and maintained on a WT background for control groups. SPNs were filled with a cesium-based internal and Alexa 594 for imaging dendrites and dendritic spines at ~910 nm (**Figure 6B-C**); the presence or absence of GFP labeling was used to assign pathway identity. Uncaging evoked EPSCs (uEPSCs) were elicited using 0.5 ms long pulses of 725 nm laser light, directed near dendritic spines (~0.5-1 µm away), in order to drive focal uncaging of MNI-glutamate. Locations of peak responses, sampled for 3 sites near each dendritic spine, were chosen for data acquisition for every synapse. Recordings were carried out in the presence of blockers of GABAARs, NMDARs, muscarinic receptors, and sodium channels, for isolation of single synapse AMPAR responses. We found that single spine glutamate uEPSCs were increased in amplitude selectively in dSPNs of RC genotype mice (GFP-, *+/RC* 196% of control, GS, 102% of control; one-way ANOVA, $p<0.05$, post hoc tests, as noted; n=18-28 dendritic spines/group) (**Figure 6D-F**). For Drd2-eGFP^{+} SPNs (iSPNs), no uEPSC amplitude differences were observed (GFP+, RC 70% of control, GS, 80% of control; one-way ANOVA, $p=0.1682$; n=21-65 dendritic spines/group), suggesting a pathway-specific effect on single synapse function in the RC genotype.

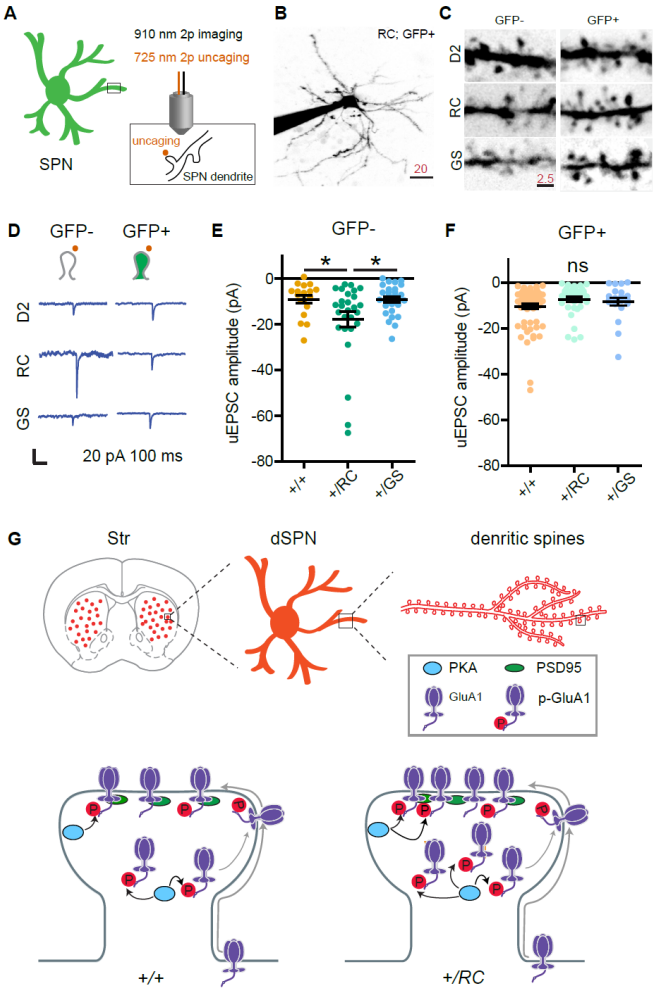

Figure 6. LRRK2 RC mutation increases glutamate uncaging-evoked currents in dSPNs.

A. Schematic illustrating experimental design. **B**. Example projection of a 2-photon laser scanning microscopy stack showing an +/RC; GFP+ SPN (iSPN). Scale bar, 20 µm. **C**. Close up images of representative dendrites from SPNs in the 6 genotype-pathway combinations, shown using inverse greyscale LUT. **D**. Example single synapse AMPA receptor mediated currents, evoked by focal uncaging of MNI-glutamate. Scale bar, 20 pA and 100 ms. **E**. Summary graph showing uncaging-evoked EPSCs (uEPSCs) for GFP- SPNs in controls, RC, and GS mutants. Asterisks reflect statistical significance for Tukey post hoc comparisons after one-way ANOVA. **F**. Same as **E**, but for GFP+ SPNs. **G**. Summary schematic for the study, illustrating changes in synaptic content of glutamate receptors in LRRK2 mutations.

DISCUSSION

In the present study, we characterized synaptic dysfunctions caused by mutant LRRK2 (RC and GS) in pathway-identified SPNs. To our knowledge, this is the first comparative approach focusing on more than one PD related LRRK2 mutation, and employing both global and single synapse approaches for the study of LRRK2 driven striatal remodeling. By studying RC and GS KI mouse lines side by side, we were able to demonstrate that the two most common LRRK2 gain of function pathogenic mutations[35] alter the function of SPN excitatory synapses in largely similar ways, with several potentially important differences. The observed changes were frequently stronger for the RC mutations, and more exaggerated in the direct pathway. For example, while whole cell electrophysiology recordings revealed decreases in the mESPCs frequency across both *+/RC* and *+/GS* mice, 2-photon dual laser glutamate uncaging and imaging, combined with whole-cell electrophysiology, demonstrated larger amplitude in uEPSCs selectively for *+/RC* dSPNs. This observation paralleled higher synaptic GluA1 receptors levels in the same subtype *+/RC* SPNs (**Figure 6G**).

Based on the current knowledge, it remains unclear why the RC mutation is associated with somewhat more pronounced effects on sculpting striatal synapses. The GS mutation, which has been the main focus of the current literature, is found in the kinase domain of LRRK2, whereas the RC mutation is located in the GTPase domain of the protein[36,37]. It has been previously proposed that all pathogenic mutations lead to increased LRRK2 kinase activity, although the mechanism by which RC does this still remains unclear[1,9]. Moreover, it is not known whether aberrant LRRK2 substrate phosphorylation is the predominant pathogenic mechanism in LRRK2 mediated striatal changes. Recent findings have revealed a subset of Rab family of proteins as the long awaited bona fide LRRK2 substrates[8]. Notably, the RC mutation, mainly in the context of heterologous cell lines, leads to higher increase in Rabs phosphorylation compared to the GS mutation, which is localized to the kinase domain[29,28]. By using Rab8A phosphorylation at T72 as a readout for LRRK2 kinase activity, our findings confirmed that RC mutation led to higher phosphorylation in synaptic striatal extracts, compared to GS. Similarly, evidence of increased synaptic PKA activities was observed in *+/RC* and not *+/GS* striatal synaptic fractions. This increased PKA activity in the RC synapses is expected to positively correlate with elevations in dSPNs signaling[38]. Specifically, phosphorylation of GluA1 at Ser 845 by PKA facilitates the targeting of the receptors to extrasynaptic membranes and their “priming” for synaptic insertion and this results in elevated GluA1 synaptic incorporation[39]. Indeed, our biochemical and SIM imaging data in RC mice support this notion. In contrast to dSPNs, PKA driven signaling

requirements for iSPNs are more complex, due to the involvement of adenosine. This molecule can be released by neurons or glia[40,41], complicating predictions for PKA involvement in mutant LRRK2 function in iSPNs.

Several prior reports demonstrate a LRRK2 mediated presynaptic regulation of glutamatergic transmission[14,15,42,43], while emerging evidence emphasizes a postsynaptic role for LRRK2[12,14]. Our previous and current findings showed that LRRK2 contributes to glutamatergic synaptic functions by directing PKA signaling events in SPNs, leading to altered GluA1 synaptic incorporation in the striatum of RC mice[12]. Despite the elevated GluA1 levels in the synapses of *+/RC* dSPNs, there were no alterations in mean mEPSCs amplitude in these neurons. However, cumulative probability analysis demonstrated that the amplitude shifted toward larger values in the *+/RC* dSPNs, suggesting an inhomogeneity of synaptic function, where a fraction of synapses exhibit larger GluA1-dependent responses and single-synapse uncaging-evoked EPSCs. This scenario, on top of overall dampening of mEPSC frequency, is expected to bias mutant dSPN responses to be driven by a narrower set of glutamatergic inputs than is normally the case. Overtime, a small bias could be amplified through the recurrent circuitry of basal ganglia loops[23]. While there are some differences in the age of preparation and in recording conditions, our consistent finding of substantial miniature EPSC frequency decreases for both mutations in pathway-identified SPNs are in disagreement with prior recordings of spontaneous events in the GS mutant mice. One recent report showed elevations in spontaneous EPSCs events frequency in GS KI mice at 1-3 months[15], while another reported changes in spontaneous but not miniature events with the GS mutation in pre-weaning mutants[14], although recordings were primarily performed in a mixed population of direct and indirect pathway SPNs, and neither study thoroughly compared the two mutations. Such differences in spontaneous event frequency point to a potential circuit-level compensatory mechanism that may be driven by disturbances in a subset of SPN excitatory synapses. Surprisingly, in the presence of clear functional and nano-architecture abnormalities, aggregate dendritic spine density and morphology, at least at the ages we evaluated, appeared normal. One possible explanation for this mismatch that requires further investigation is the possibility of higher occurrence of nonfunctional or differently functioning spines in LRRK2 mutant SPNs.

Given the critical role of LRRK2 in excitatory glutamatergic synapses[12,15,14], a more nuanced understanding of LRRK2 mediated synaptic alterations should facilitate the search for more targeted PD therapies. Here, we focused primarily on interrogating cell type specific LRRK2

based responses. Why does this pathway specificity matter? It is well-established that dopamine loss causes pathway specific morphological and functional changes in SPNs[21,22,44]. Moreover, dSPNs and iSPNs exhibit opposing PKA pathway signaling properties after dopamine receptor activation[45,40]. Given the critical role of LRRK2 in synaptic PKA activities[12,46], these mutations are poised to have pathway specific effects and present distinct opportunities for pathway-targeted therapies.

Over the past years, a number of transgenic mouse models was generated to study LRRK2 function[47,48] however the results were found to be inconsistent across studies. Gene-targeted mutant LRRK2 KI mice represent the most physiologically relevant model to investigate LRRK2 mediated alterations and unravel disease mechanisms. Here, we attempt to synthesize and further the existing knowledge by employing a comparative approach focusing on two distinct mutations, combined with a powerful suite of techniques allowing for both global and single synapse study of LRRK2 SPNs. Our conclusions provide useful insights on how LRRK2 mutations could confer PD susceptibility for human patients with otherwise sub-clinical alterations in dopamine signaling. This is of particular interest as asymptomatic mutant LRRK2 carriers show early corticostriatal connectivity changes[49,50,51], in the absence of neuronal degeneration. Therefore, KI LRRK2 mouse models expressing pathogenic mutations represent valuable models that enable investigations of early events that precede neuronal death and may be predictive of future dysfunction.

METHODS

Mouse strains and genotyping. All mouse related experiments followed the guidelines approved by the Northwestern University Animal Care and Use Committee. Young adult male and female mice (postnatal days 30-50) were used in this study. Approximately equal numbers of males and females were used for every experiment. All mice were group-housed, with standard feeding, light-dark cycle, and enrichment procedures. C57BL/6 (wild-type), *RC*[52]*, and GS*[53] heterozygous knock in mice were used for subcellular fractionation experiments. For electrophysiological and imaging approaches *RC* or *GS* mice were crossed with *Drd1α-dTomato* and/or *Drd2-eGFP* mice. Heterozygotes *for RC and GS* allele and hemizygotes for *Drd1α-dTomato* and/or *Drd2-eGFP* were used in all experiments. For dendritic spine analysis, hemizygous *Drd1-Cre*, and *Adora2a-Cre* mice crossed with RC and GS KI mice were used. All animals were backcrossed to C57BL/6 for several generations.

Subcellular fractionation and Western blot analysis

Subcellular fractionation of mouse striatum was performed as previously described[25,12] (**Figure 1B**). Specifically, mouse striata were dissected (3 striata per experiment were pooled) and rapidly homogenized in four volumes of ice-cold Buffer A (0.32 M sucrose, 5 mM HEPES, pH7.4, 1 mM $MgCl_2$, 0.5 mM $CaCl_2$) supplemented with Halt™ protease and phosphatase inhibitor cocktail (Thermo) using a Teflon homogenizer (12 strokes). Homogenized brain extract was centrifuged at 1,400 *g* for 10 min. Supernatant (S1) was saved and pellet (P1) was homogenized in buffer A with a Teflon homogenizer (5 strokes). After centrifugation at 700 *g* for 10 min, the supernatant (S1') was pooled with S1. Pooled S1 and S1′ were centrifuged at 13,800 *g* for 10 min to the crude synaptosomal pellet (P2) and the supernatant (S2). P2 was resuspended in Buffer B (0.32 M sucrose, 6 mM Tris, pH 8.0) supplemented with protease and phosphatase inhibitors cocktail with Teflon homogenizer (five strokes) and was carefully loaded onto a discontinuous sucrose gradient (0.8 M/1 M/1.2 M sucrose solution in 6 mM Tris, pH 8.0) with a Pasteur pippete, followed by centrifugation in a swinging bucket rotor for 2 h at 82,500 *g*. The synaptic plasma membrane fraction (SPM) in the interphase between 1 M and 1.2 M sucrose fractions was collected using a syringe and transferred to clean ultracentrifuge tubes. 6 mM Tris buffer was added to each sample to adjust the sucrose concentration from 1.2 M to 0.32 M and the samples were centrifuged in a swinging bucket rotor at 200,000 g for 30 min. The supernatant was removed and discarded and the SPM pellet was resuspended in 500 µl of 6mM Tris / 2 mM EDTA / 0.5% Triton X-100 solution and rotated for 30 min at 4°C. In turn, the samples were centrifuged at 32,800 *g* for 20 min. The supernatant contains the Triton soluble fraction (TSF), whereas the pellet represents the postsynaptic pellet (PSD).

S1, P2, presynaptic and PSD fractions were separated by 4–12% NuPage Bis-Tris PAGE (Invitrogen) and transferred to membranes using the iBlot nitrocellulose membrane Blotting system (Invitrogen) by following manufacture protocol. Primary antibodies specific for GluA1 (Cell Signaling Technology #13185), pGluA1 (Cell Signaling Technology #8084), phospho-PKA substrates (Cell Signaling Technologies #9624), phospho-Rab8A (Abcam, ab188574) and total Rab 8A (Abcam, ab230260) , as well as secondary anti-mouse and anti-rabbit (Thermo Fischer Scientific) Membranes were incubated with Immobilon® ECL Ultra Western HRP Substrate (Millipore) for 3 minutes prior to image acquisition. Chemiluminescent blots were imaged with iBright™ CL1000 imaging system (Thermo Fisher Scientific). For quantitative analysis, images were analyzed using iBright Analysis Software (Thermo Fisher Scientific).

<u>Primary neuronal cultures</u>

Primary corticostriatal co-cultures were prepared as described previously[12,54]. In brief, striatal cultures were prepared from P0 pups of *Drd1-Tomato* or *Drd2-eGFP* mice crossed with mutant KI LRRK2 lines (*G2019S* and *R1441C*). Tissues were digested by papain (Worthington Biochemical Corporation) and the striatal and cortical cells were mixed at a ratio of 1:2. The neurons were placed on coveslips with plating medium (Medium I) containing Basal Eagle Medium (Sigma-Aldrich) supplemented with 1 x GlutaMAXTM-I (Gibco™), 1 × B27 (Gibco™), 1 x N-2 (Gibco™), 1 x Antibiotic Antimycotic (Sigma-Aldrich), 5% horse serum (Gibco™) and 5% FBS (Gibco™) at a density of $4x10^5$ for about one hour. After initial plating, medium was changed to Medium I without the horse serum and the FBS supplemented with 2.5 μM arabinosylcytosine (Sigma-Aldrich) (Medium II). Half of the medium was changed with fresh Medium II every 7 days; experiments were conducted 28-30 days after plating.

SIM imaging and analysis

Multichannel SIM images were obtained with a Nikon Structured Illumination super-resolution microscope using a 100x, 1.4 NA objective as previously described[33]. The acquisition was set to 10 MHz, 16 bit depth with EM gain and no binning. Exposure was between 100-500 ms and the EM gain multiplier restrained below 1500. Conversion gain was held at 1x. Laser power was adjusted to keep LUTs within the first quarter of the scale. Single images were processed and analyzed using Nikon Elements software. Reconstruction parameters (Illumination Modulation Contrast, High Resolution Noise Suppression, and Out of Focus Blur Suppression) (0.94, 0.98, and 0.07) for GluA1/ PSD95 and (1.2, 3.0 and 0.07) for GFP/tdTomato were kept consistent across all acquisitions and experiments. Single spine analyses were carried out on 72-95 spines across 9-12 neurons per genotype. Images of dendritic fragments were collected from secondary to tertiary dendrites across genotypes. All the spines on the fragments were analyzed. GFP/tdTomato signal (Thermo Fischer Scientific, #A10262/#M11217) was used to generate a mask to identify the spine shape, subsequent analysis were done with the nanodomains of GluA1 (NeuroMab #75327) and PSD95 (Thermo Fischer Scientific, #51-6900)within the mask. 3D reconstructions in a single plane used 9 images captured with 2D SIM and reconstructed with 3D SIM utilizes 15 to increase xy and z resolution were generated by Nikon Element and the illumination modulation contrast was set automatically by the software. Nikon Elements software (general analysis) was used for quantification of colocalization of GluA1 and PSD95 proteins. The images were thresholded for each channel and kept constant across experiments. The regions of interest (puncta) were outlined, and total immunofluorescence number and binary area for each region per channel were measured automatically. Regions in one channel were overlayed on the

other channel. The minimum distances between puncta (e.g. PSD95 to GluA1) were measured from surface to surface automatically by the software.

Intracranial injections

Intracranial injections were performed as previously described[23]. Briefly, P4-5-day-old pups were placed into a stereotaxic frame under cryoanesthesia. 200 nl of AAV8/Flex-GFP virus ($6.2*10^{12}$ used at 1:3 dilution, UNC Vector Core, Chapel Hill, NC) were delivered into the dorsal striatum at a rate of 100 nl min^{-1} using microprocessor-based controller, Micro4 (WPI). In order to ensure targeting of the dorsal striatum the needle was placed 1 mm anterior to midpoint between ear and eye, 1.5 mm from midline and 1.8 mm ventral to brain surface.

Confocal microscopy and dendritic spine analysis

Confocal images of fixed 80 µm thick brain sections of P30 pups injected with the AAV8/Flex-GFP virus were obtained with the Nikon A1R scope. Fluorescence projection images of dendrites and the corresponding spines were acquired with a 60x oil immersion objective (NA=1.4) at 0.1 µm intervals with 1024x1024 pixel resolution. For each genotype, 2-4 segments per neuron, 9-14 neurons from 3-4 animals were used to generate z-stacks. Fragments between secondary to tertiary dendrites without overlap with other neurons or discontinuous were chosen for analysis. Dendritic spine density and morphology was performed using Imaris 9.21 software (Bitplane, Concord, USA). Images of dendritic fragments were collected from secondary to tertiary dendrites, for tracing of the dendritic fragments the autopath mode of the filament tracer and default settings were selected. The following settings were used for spine detection: 0.5 µm minimal head size, 1.8 µm maximum length, seed point threshold approx. 10, no branched spines were allowed. Spine detection was manually corrected if necessary. Classification of spines into stubby, mushroom-like and filopodia was performed using the Imaris XTension classify spines with following definitions: stubby: spine length < 0.75 µm; mushroom: spine length < 3.5µm, spine head width >0.35 µm and spine head width > spine neck width; filopodia: when it did not fit the criteria mentioned above[55].

Electrophysiological recordings

Two hundred and fifty µm thick acute coronal brain slices were prepared as described previously[34, 56] and incubated in artificial cerebral spinal fluid (ACSF) containing (in mM) 127 NaCl, 2.5 KCl, 25 $NaHCO_3$, 1.25 NaH_2PO_4, 2.0 $CaCl_2$, 1.0 $MgCl_2$, and 25 glucose (osmolarity ~310 mOsm/L). Slices were recovered at 34ºC for 15 min, followed by 30 min at RT, and transferred to

a recording chamber perfused with oxygenated ACSF at a flow rate of 2–3 mL/min. Whole-cell recordings were obtained from dorsolateral striatal neurons visualized under infrared Dodt or DIC contrast video microscopy using patch pipettes of ~4-6 MΩ resistance. Drd2 BAC GFP signal visualized under epifluorescence was used to target iSPNs, while Drd2 GFP-negative neurons with electrophysiological properties of SPNs were considered dSPNs. Both fluorescent and non-fluorescent neurons were targeted for recording. Internal solution consisted of (in mM): 120 $CsMeSO_4$, 15 CsCl, 10 HEPES, 2 QX-314 Chloride, 2 Mg-ATP, 0.3 Na-GTP, 1 EGTA (pH ~7.2, ~295 mOsm). Morphology was confirmed using 20 µM Alexa 594 in the recording pipette. Recordings were made using a Multiclamp 700B amplifier (Molecular Devices). Data were sampled at 10 kHz and filtered at 4 kHz, acquired in MATLAB (MathWorks). Series resistance, measured with a 5 mV hyperpolarizing pulse in voltage clamp, was under 30 MΩ and was left uncompensated. Miniature EPSCs were recorded from voltage clamped SPNs held at -70 mV in the absence of stimulation. Over 2 minutes of recording per neuron was used for analyses. For recordings of miniature EPSCs, 50 µM gabazine, 10 µM scopolamine, 10µM CPP, and 1 µM TTX were added to the ACSF.

Two-photon imaging and uncaging

Two-photon laser-scanning microscopy and two-photon laser photoactivation were accomplished on a modified Scientifica microscope with a 60X (1.0 NA) objective. Two mode-locked Ti:Sapphire lasers (Mai-Tai eHP Deep See and Mai-Tai eHP; Spectra Physics) were separately tuned, with beam power controlled by independent Pockels cells (ConOptics). The beams were separately shuttered, recombined using a polarization-sensitive beam-splitting cube (Thorlabs), and guided into the same galvanometer scanhead (Cambridge). The Mai Tai eHP Deep See was tuned to ~910 nm for excitation of genetically encoded GFP and Alexa 594, and the Mai Tai eHP was tuned to 725nm for photoactivation of recirculated caged MNI-L-glutamate (2 mM, Tocris)[57,58]. Neurons in the dorsolateral striatum were targeted for recording, as for other electrophysiology assays, with secondary and tertiary dendrites targeted for uncaging. All 2P uncaging voltage clamp recordings were made at a holding potential of −70 mV. Internal solution contained (in mM) 115 K-gluconate, 20 KCl, 4 $MgCl_2$, 10 HEPES, 4 Mg-ATP, 0.3 Na-GTP, 7 phosphocreatine, 0.1 EGTA, (pH 7.2, 290 mOSm). Alexa Fluor 594 (10–20 µM) was added to the internal solution to visualize cell morphology for uncaging/imaging with physiology experiments. Uncaging evoked EPSCs were elicited by 0.5 ms pulses of 725 nm laser light (~20 mW at the focal plane). Up to three locations in a single field of view were stimulated (1 sec apart) in a single sweep. Stimulation of a single location occurred with a minimum 10 sec ISI. A spot diameter of ≤0.8 µm, based on

measurements of 0.5 µm beads (17152-10; Polysciences Inc.) was used for all 2-photon laser flash photolysis experiments. Two GaAsP photosensors (Hamamatsu, H7422) with 520/28 nm band pass filters (Semrock), mounted above and below the sample, were used for imaging fluorescence signals. A modified version of ScanImage was used for data acquisition[59,34].

Statistical analyses

Group statistical analyses were done using GraphPad Prism 7 software (GraphPad, LaJolla, CA). For n sizes, both the number of trials recorded and the number of animals are provided. All data are expressed as mean + SEM, or individual plots. For two-group comparisons, statistical significance was determined by two-tailed Student's t-tests. For multiple group comparisons, one-way analysis of variance (ANOVA) tests were used for normally distributed data, followed by post hoc analyses. For non-normally distributed data, non-parametric tests for the appropriate group numbers were used, such as Mann-Whitney and Kruskal-Wallis. Spearman correlation was used to detect correlation between two groups of data. $p<0.05$ was considered statistically significant.

ACKNOWLEDGEMENTS

This work was supported by Michael J. Fox Foundation for Parkinson's Research (LP), NIH R01 NS097901 (LP), NINDS R01 NS107539 (YK), Rita Allen Foundation Scholar Award (YK), Searle Scholar Award (YK), and Beckman Young Investigator Award (YK). NB was supported by NINDS F32 NS103243. The authors are grateful to Lindsey Butler for mouse colony management. We also thank Dr. Heather Melrose for providing the LRRK2 G2019S knock-in mice.

AUTHOR CONTRIBUTIONS

Y.K. and L.P. designed and supervised the experiments. C.C. performed biochemical experiments, SIM analysis, neonatal injections, and dendritic spine analysis. G.S. performed ex vivo electrophysiology. N.B conducted 2-photon laser scanning microscopy and glutamate uncaging experiments. S.K. maintained the mouse colony and carried out imaging data analysis. Y.K and L.P wrote the manuscript with substantial contribution from all co-authors.

REFERENCES

1. Alessi, D. R. & Sammler, E. LRRK2 kinase in Parkinson's disease. *Science* **360**, 36–37 (2018).

2. Kluss, J. H., Mamais, A. & Cookson, M. R. LRRK2 links genetic and sporadic Parkinson's disease. *Biochemical Society Transactions* **47**, 651–661 (2019).

3. Di Fonzo, A. *et al.* Comprehensive analysis of the LRRK2 gene in sixty families with Parkinson's disease. *Eur. J. Hum. Genet.* **14**, 322–31 (2006).

4. Haugarvoll, K. *et al.* Lrrk2 R1441C parkinsonism is clinically similar to sporadic Parkinson disease. *Neurology* **70**, 1456–60 (2008).

5. Di Maio, R. *et al.* LRRK2 activation in idiopathic Parkinson's disease. *Sci Transl Med* **10**, (2018).

6. Cookson, M. R. The role of leucine-rich repeat kinase 2 (LRRK2) in Parkinson's disease. *Nat Rev Neurosci* **11**, 791–797 (2010).

7. Esteves, A. R., Swerdlow, R. H. & Cardoso, S. M. LRRK2, a puzzling protein: insights into Parkinson's disease pathogenesis. *Exp. Neurol.* **261**, 206–16 (2014).

8. Steger, M. *et al.* Phosphoproteomics reveals that Parkinson's disease kinase LRRK2 regulates a subset of Rab GTPases. *Elife* **5**, (2016).

9. Nguyen, A. P. T. & Moore, D. J. Understanding the GTPase activity of LRRK2: Regulation, function, and neurotoxicity. in *Advances in Neurobiology* **14**, 71–88 (Springer New York LLC, 2017).

10. Xiong, Y. *et al.* GTPase activity plays a key role in the pathobiology of LRRK2. *PLoS Genet* **6**, e1000902 (2010).

11. West, A. B. *et al.* Differential LRRK2 expression in the cortex, striatum, and substantia nigra in transgenic and nontransgenic rodents. *J. Comp. Neurol.* **522**, 2465–2480 (2014).

12. Parisiadou, L. *et al.* LRRK2 regulates synaptogenesis and dopamine receptor activation through modulation of PKA activity. *Nat Neurosci* **17**, 367–376 (2014).

13. Beccano-Kelly, D. A. *et al.* LRRK2 overexpression alters glutamatergic presynaptic plasticity, striatal dopamine tone, postsynaptic signal transduction, motor activity and memory. *Hum. Mol. Genet.* **24**, 1336–49 (2015).

14. Matikainen-Ankney, B. A. *et al.* Altered Development of Synapse Structure and Function in Striatum Caused by Parkinson's Disease-Linked LRRK2-G2019S Mutation. *J Neurosci* **36**, 7128–7141 (2016).

15. Volta, M. *et al.* Initial elevations in glutamate and dopamine neurotransmission decline with age, as does exploratory behavior, in LRRK2 G2019S knock-in mice. *Elife* **6**, (2017).

16. Pan, P. Y. *et al.* Parkinson's disease-associated LRRK2 hyperactive kinase mutant disrupts synaptic vesicle trafficking in ventral midbrain neurons. *J. Neurosci.* **37**, 11366–11376 (2017).

17. Matikainen-Ankney, B. A. *et al.* Parkinson's Disease-Linked LRRK2-G2019S Mutation Alters Synaptic Plasticity and Promotes Resilience to Chronic Social Stress in Young Adulthood. *J Neurosci* **38**, 9700–9711 (2018).

18. Huntley, G. W. LRRK2 mutation alters behavioral, synaptic and non-synaptic adaptations to acute social stress. *bioRxiv* 2020.02.25.965194 (2020). doi:10.1101/2020.02.25.965194

19. West, A. B. *et al.* Differential LRRK2 expression in the cortex, striatum, and substantia nigra in transgenic and nontransgenic rodents. *J. Comp. Neurol.* **522**, 2465–80 (2014).

20. Giesert, F. *et al.* Expression Analysis of Lrrk1, Lrrk2 and Lrrk2 Splice Variants in Mice. *PLoS One* **8**, e63778 (2013).

21. Kravitz, A. V. *et al.* Regulation of parkinsonian motor behaviours by optogenetic control of basal ganglia circuitry. *Nature* **466**, 622–626 (2010).

22. Fieblinger, T. *et al.* Cell type-specific plasticity of striatal projection neurons in parkinsonism and L-DOPA-induced dyskinesia. *Nat. Commun.* **5**, (2014).

23. Kozorovitskiy, Y., Saunders, A., Johnson, C. A., Lowell, B. B. & Sabatini, B. L. Recurrent network activity drives striatal synaptogenesis. *Nature* **485**, 646–650 (2012).

24. Tozzi, A. *et al.* Dopamine D2 receptor activation potently inhibits striatal glutamatergic transmission in a G2019S LRRK2 genetic model of Parkinson's disease. *Neurobiol. Dis.* **118**, 1–8 (2018).

25. Bermejo, M. K., Milenkovic, M., Salahpour, A. & Ramsey, A. J. Preparation of synaptic plasma membrane and postsynaptic density proteins using a discontinuous sucrose gradient. *J. Vis. Exp.* (2014). doi:10.3791/51896

26. Peng, J. *et al.* Semiquantitative proteomic analysis of rat forebrain postsynaptic density fractions by mass spectrometry. *J. Biol. Chem.* **279**, 21003–11 (2004).

27. Bonet-Ponce, L. & Cookson, M. R. The role of Rab GTPases in the pathobiology of Parkinson' disease. *Current Opinion in Cell Biology* **59**, 73–80 (2019).

28. Purlyte, E. *et al.* Rab29 activation of the Parkinson's disease-associated LRRK2 kinase. *EMBO J.* **37**, 1–18 (2018).

29. Liu, Z. *et al.* LRRK2 phosphorylates membrane-bound Rabs and is activated by GTP-bound Rab7L1 to promote recruitment to the trans-Golgi network. *Hum. Mol. Genet.* **27**, 385–395 (2018).

30. Roche, K. W., O'Brien, R. J., Mammen, A. L., Bernhardt, J. & Huganir, R. L. Characterization of multiple phosphorylation sites on the AMPA receptor GluR1 subunit. *Neuron* **16**, 1179–1188 (1996).

31. Gao, R. *et al.* CNTNAP2 stabilizes interneuron dendritic arbors through CASK. *Mol. Psychiatry* **23**, 1832–1850 (2018).

32. Crosby, K. C. *et al.* Nanoscale Subsynaptic Domains Underlie the Organization of the Inhibitory Synapse. *Cell Rep.* **26**, 3284–3297.e3 (2019).

33. Smith, K. R. *et al.* Psychiatric Risk Factor ANK3/Ankyrin-G Nanodomains Regulate the Structure and Function of Glutamatergic Synapses. *Neuron* **84**, 399–415 (2014).

34. Kozorovitskiy, Y., Peixoto, R., Wang, W., Saunders, A. & Sabatini, B. L. B. L. Neuromodulation of excitatory synaptogenesis in striatal development. *Elife* **4**, pii: e10111. (2015).

35. Hernandez, D. G., Reed, X. & Singleton, A. B. Genetics in Parkinson disease: Mendelian versus non-Mendelian inheritance. *Journal of Neurochemistry* 59–74 (2016). doi:10.1111/jnc.13593

36. Paisán-Ruiz, C., Lewis, P. A. & Singleton, A. B. LRRK2: Cause, risk, and mechanism. *Journal of Parkinson's Disease* **3**, 85–103 (2013).

37. Cookson, M. R. Cellular effects of LRRK2 mutations. *Biochemical Society Transactions* **40**, 1070–1073 (2012).

38. Zhai, S., Shen, W., Graves, S. M. & Surmeier, D. J. Dopaminergic modulation of striatal function and Parkinson's disease. *Journal of Neural Transmission* (2019). doi:10.1007/s00702-019-01997-y

39. Diering, G. H. & Huganir, R. L. The AMPA Receptor Code of Synaptic Plasticity. *Neuron* **100**, 314–329 (2018).

40. Surmeier, D. J., Ding, J., Day, M., Wang, Z. & Shen, W. D1 and D2 dopamine-receptor modulation of striatal glutamatergic signaling in striatal medium spiny neurons. *Trends in Neurosciences* **30**, 228–235 (2007).

41. Zhang, X. *et al.* Balance between dopamine and adenosine signals regulates the PKA/Rap1 pathway in striatal medium spiny neurons. *Neurochem. Int.* **122**, 8–18 (2019).

42. Beccano-Kelly, D. A. *et al.* LRRK2 overexpression alters glutamatergic presynaptic plasticity, striatal dopamine tone, postsynaptic signal transduction, motor activity and memory. *Hum Mol Genet* **24**, 1336–1349 (2015).

43. Piccoli, G. *et al.* LRRK2 controls synaptic vesicle storage and mobilization within the recycling pool. *J. Neurosci.* **31**, 2225–37 (2011).

44. Gertler, T. S., Chan, C. S. & Surmeier, D. J. Dichotomous anatomical properties of adult striatal medium spiny neurons. *J. Neurosci.* **28**, 10814–10824 (2008).

45. Gerfen, C. R. & Surmeier, D. J. Modulation of Striatal Projection Systems by Dopamine. *Annu. Rev. Neurosci.* **34**, 441–466 (2011).

46. Tozzi, A. *et al.* Dopamine D2 receptor-mediated neuroprotection in a G2019S Lrrk2 genetic model of Parkinson's disease. *Cell Death Dis.* **9**, (2018).

47. Volta, M. & Melrose, H. LRRK2 mouse models: Dissecting the behavior, striatal neurochemistry and neurophysiology of PD pathogenesis. *Biochemical Society Transactions* **45**, 113–122 (2017).

48. Xiong, Y., Dawson, T. M. & Dawson, V. L. Models of LRRK2-associated parkinson's disease. in *Advances in Neurobiology* **14**, 163–191 (Springer New York LLC, 2017).

49. Helmich, R. C. *et al.* Reorganization of corticostriatal circuits in healthy G2019S LRRK2 carriers. *Neurology* **84**, 399–406 (2015).

50. Vilas, D. *et al.* Clinical and imaging markers in premotor LRRK2 G2019S mutation carriers. *Parkinsonism Relat. Disord.* **21**, 1170–6 (2015).

51. Vilas, D. *et al.* Nigral and striatal connectivity alterations in asymptomatic LRRK2 mutation carriers: A magnetic resonance imaging study. *Mov. Disord.* **31**, 1820–1828 (2016).

52. Tong, Y. *et al.* R1441C mutation in LRRK2 impairs dopaminergic neurotransmission in mice. *Proc. Natl. Acad. Sci.* **106**, 14622–14627 (2009).

53. Yue, M. *et al.* Progressive dopaminergic alterations and mitochondrial abnormalities in LRRK2 G2019S knock-in mice. *Neurobiol. Dis.* **78**, 172–95 (2015).

54. Tian, X., Kai, L., Hockberger, P. E., Wokosin, D. L. & Surmeier, D. J. MEF-2 regulates activity-dependent spine loss in striatopallidal medium spiny neurons. *Mol. Cell. Neurosci.* **44**, 94–108 (2010).

55. Schier, C. J. *et al.* Selective vulnerability of striatal D2 versus D1 dopamine receptor-expressing medium spiny neurons in HIV-1 Tat transgenic male mice. *J. Neurosci.* **37**, 5758–5769 (2017).

56. Xiao, L., Priest, M. F., Nasenbeny, J., Lu, T. & Kozorovitskiy, Y. Biased Oxytocinergic Modulation of Midbrain Dopamine Systems. *Neuron* **95**, 368–384.e5 (2017).

57. Xiao, L., Priest, M. F. & Kozorovitskiy, Y. Oxytocin functions as a spatiotemporal filter for excitatory synaptic inputs to VTA dopamine neurons. *Elife* **7**, (2018).

58. Banala, S. *et al.* Photoactivatable drugs for nicotinic optopharmacology. *Nat. Methods* **15**, 347–350 (2018).

59. Pologruto, T. A., Sabatini, B. L. & Svoboda, K. ScanImage: Flexible software for operating laser scanning microscopes. *Biomed. Eng. Online* **2**, (2003).